Compact high-resolution spaceborne echelle grating spectrometer with acousto-optical tunable filter based order sorting for the infrared domain from 2.2 to 4.3 μm

Dennis Nevejans, Eddy Neefs, Emiel Van Ransbeeck, Sophie Berkenbosch, Roland Clairquin, Lieve De Vos, Wouter Moelans, Stijn Glorieux, Ann Baeke, Oleg Korablev, Imant Vinogradov, Yuri Kalinnikov, Benny Bach, Jean-Pierre Dubois, and Eric Villard

A new compact spaceborne high-resolution spectrometer developed for the European Space Agency's Venus Express spacecraft is described. It operates in the IR wavelength range of 2.2 to 4.3 μm and measures absorption spectra of minor constituents in the Venusian atmosphere. It uses a novel echelle grating with a groove density of 4 lines/mm in a Littrow configuration in combination with an IR acousto-optic tunable filter for order sorting and an actively cooled HgCdTe focal plane array of 256 by 320 pixels. It is designed to obtain an instrument line profile of 0.2 cm^{-1}. First results on optical and spectral properties are reported.

OCIS codes: 350.6090, 120.6200, 010.1280, 230.1040, 230.1950, 300.6190.

1. Introduction

Until now, all IR optical spectrometers flown on board spacecraft sent to measure absorption spectra in the atmospheres of solar system planets were limited to spectral resolutions of 1 cm^{-1} or worse, which has seriously hampered the detection of minor atmospheric species. A typical example is the Planetary Fourier Spectrometer[1,2] (PFS), an instrument now operating on board the European Space Agency (ESA) Mars Express and Venus Express spacecraft. Its unapodized spectral resolution is limited to 1–2 cm^{-1}. Spectrometers[3] on earlier planetary missions, such as Voyager and Mariner 9, were Fourier transform spectrometers (FTS) that had even lower resolutions, ranging from 2.4 to 5 cm^{-1}. These resolutions were much lower than those of optical spectrometers observing the Earth's atmosphere from orbit: e.g., an older Earth-orbiting spectrometer such as the Atmospheric Trace Molecule Spectroscopy instrument[4] (ATMOS) had an unapodized resolution of 0.125 cm^{-1}, and the recent Atmospheric Chemistry Experiment[5] (ACEFTS) has one of 0.025 cm^{-1}. Ground-based instruments easily reach ten times better resolution. All these high-resolution IR spectrometers are bulky instruments, however, making it difficult to install them on planetary or interplanetary spacecraft that have limited resources.

For the ESA Venus Express (VEX) mission to planet Venus a compact IR spectrometer that has low mass, high throughput, rather high resolution (10 times better than the PFS), a rather large free spectral range (~20 cm^{-1}), and a spectral sampling interval and an instrument line profile of 0.1 and 0.2 cm^{-1}, respectively, was envisaged. These requirements can be fulfilled by combining a highly dispersive element operated at high diffraction orders (a coarse-spaced echelle grating) with a diffraction order sorting device. Instead of selecting grating orders by means of interchangeable bandpass filters on a rotating filter wheel (e.g., the Cryogenic Echelle Spectrograph of the NASA Infrared Telescope Facility) or by means of

D. Nevejans (dennis.nevejans@bira-iasb.be), E. Neefs, E. Van Ransbeeck, S. Berkenbosch, and R. Clairquin are with the Belgian Institute for Space Aeronomy (BIRA-IASB), Ringlaan 3 B-1180 Brussels, Belgium. L. De Vos, W. Moelans, S. Glorieux, and A. Baeke are with OIP Sensor Systems, Westerring 21, B-9700 Oudenaarde, Belgium. O. Korablev and I. Vinogradov are with the Space Research Institute (IKI), 117997, 84/32 Profsoyuznaya Street, Moscow, Russia. Y. Kalinnikov is with the AFAR, NPO SPURT, 141570, Zelenograd, Moscow Region, Russia. B. Bach is with the Bach Research Corporation, Suite D, Boulder, Colorado 80301. J.-P. Dubois and E. Villard are with the Service d'Aéronomie du Centre National de la Recherche Scientifique, B.P. 3, F-91371 Verrières le Buisson Cédex, France.

Received 23 November 2005; revised 5 March 2006; accepted 6 March 2006; posted 13 March 2006 (Doc. ID 66222).

0003-6935/06/215191-16$15.00/0

an orthogonal cross dispersing element, as in the Visible and Infra Red Thermal Imaging Spectrometer[6] (VIRTIS) on the ESA Rosetta, Mars Express, and Venus Express spacecraft), one can implement order filtering by inserting an in-line acousto-optic device, known as an acousto-optical tunable filter (AOTF) that may be considered an electronically tunable constant-bandwidth bandpass filter.

A first echelle–AOTF combination for the UV–visible (200 to 425 nm) wavelength range was reported in the literature in 1999. This Compact High Resolution Spectrometer[7–9] (CHRS) yielded a spectral resolution of 0.004 to 0.008 nm and an approximately tenfold reduction in size and weight compared with competing baseline instruments that provide comparable resolution. The authors[7–9] claim that it also offers less-complex spectrum detection and interpretation than the configuration of an echelle combined with orthogonal dispersion.

The working principle of the echelle–AOTF combination has since then been extended to the near-IR range of wavelengths and has been demonstrated in two implementations: one[10,11], covering the wavelength range from 1 to 1.65 μm with a resolving power of 30,000, manufactured, assembled, and tested by a joint French–Russian team [Service d'Aéronomie and the Russian Space Research Institute (IKI)], and another that was intended as a precursor for the spaceborne IR spectrometer described in this paper, built by the Belgian Institute for Space Aeronomy (BIRA-IASB) and its industrial partner OIP Sensor Systems (OIP), Oudenaarde, Belgium. In this paper we describe an echelle-based spectrometer with AOTF order sorting based on the same basic principles but specifically designed for the 2.2 to 4.3 μm range in the IR. This high-resolution spectrometer,[12–15] called Solar Occultation in the IR (SOIR), was accepted as part of the scientific payload for the VEX mission of the ESA. A detailed optical study and design as well the manufacture of the instrument were performed by OIP in association with BIRA-IASB.

2. Summary of Scientific Goals for the Venus Express Mission

This spectrometer fits within the defined scientific mission themes[16] of the ESA VEX mission, such as the study of the dynamics, structure, composition, and chemistry of the Venusian atmosphere, and is highly appropriate for the investigation of the altitude range from 110 to 60 km. The application in the Venusian atmosphere of the solar occultation technique, for which this instrument is particularly designed, is limited because of the existence between altitudes from 45 to 70 km of thick cloud layers composed of fine droplets of sulfuric acid. However, above these cloud layers the sounding of the atmosphere and the measurement of the vertical abundance profiles of atmospheric constituents is perfectly feasible up to high altitudes.

One of the key scientific themes of the VEX mission is the understanding of the past and present water balance in the Venusian atmosphere. The study of the water escape from Venus by means of the measurement of HDO and H_2O profiles is therefore of utmost importance. Absorption lines of HDO and H_2O of the dark side of Venus have been observed from Earth in the interval 2.34 to 2.43 μm with a resolving power of 0.23 cm^{-1}, which is comparable to the resolving power offered by the instrument described. These results[17] suggest pronounced deuterium enrichment in the atmosphere of Venus, expressed by an abundance ratio D/H that is ~120 times larger than the telluric ratio. The measurement of the HDO escape profile from 60 to 80–90 km altitude by the SOIR on the VEX could confirm or refute this ground based observation.

Besides the quest for HDO, another important scientific objective for the SOIR is the measurement of the water vapor abundance profile up to 100 km, in either the 2560–2570 cm^{-1} (3.9 μm) band or the stronger 3760–3860 cm^{-1} (2.56 μm) absorption band. Other minor molecular components such as H_2, O_2, CO, sulfuric compounds like H_2S, COS, and SO_2, and acid vapors like HCl and HF are certainly present and detectable, as gas chromatographic *in situ* abundance measurements by the Venera probes[18,19] and observations from ground have shown. Also, the detection of minor constituents of the Venusian atmosphere associated with small absorption features, such as C_2H_2, CH_4, NO, N_2O, H_2CO, and HCN, will be attempted.

Finally, one can derive the Venusian atmosphere's density profile by measuring the density of its major component. By recording CO_2 absorption lines in the 4.3 μm band one can cover at once a large part of the whole altitude range from 60 to 120 km, and probably beyond.

3. Spectrometer Design Objectives

The first opportunity to design and manufacture an echelle-based high-resolution spectrometer with AOTF order sorting for the 2.2 to 4.3 μm range in the IR appeared when the ESA VEX mission was announced. The payload on board the Venus Express spacecraft comprises mainly upgraded versions of instruments already flown on the Mars Express (MEX) and Rosetta platforms, with some new instruments added. The SOIR instrument (Fig. 1) described in this paper is to be considered a new extension on top of the existing SPICAM-L experiment flown on the MEX. The combination of both is called the SPICAV.

In accordance with the scientific objectives the SOIR design was tuned for solar occultation observations of the Venusian atmosphere in the 2 to 5 μm band, a requirement that was relaxed to the wavelength range of 2.325 to 4.25 μm because of limitations imposed by the optics and the detector.

A second requirement was to achieve a spectral resolution that was ~10 times better than could be reached before for equal size and mass. An instrument line profile (ILP), with a FWHM, of 0.2 cm^{-1} and a sampling interval of 0.1 cm^{-1}/pixel over the whole spectral range, were therefore put forward.

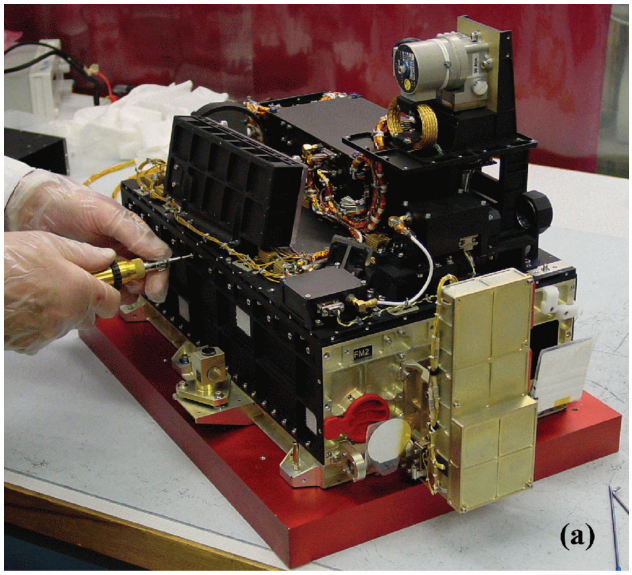

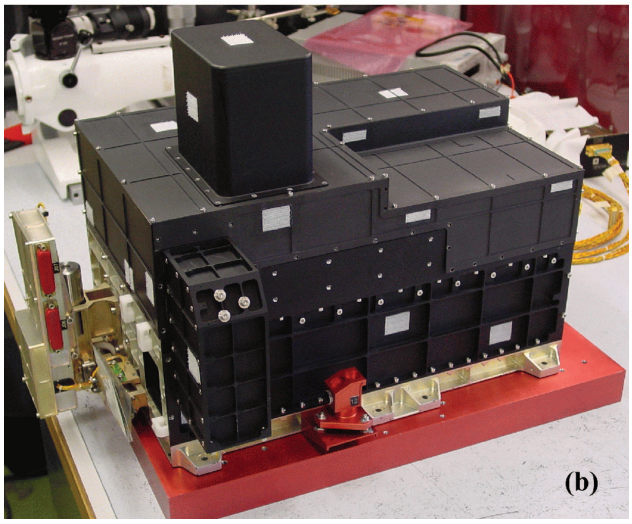

Fig. 1. Photographs of the SOIR high-resolution spectrometer mounted on top of the SPICAM-L part of the SPICAV experiment for the VEX: (a) SOIR without protective covers and periscope; (b) SOIR with protective covers and periscope installed.

This will allow deriving the density profile of already known atmospheric constituents at higher altitudes than feasible before; it will also allow the detection of yet unknown atmospheric constituents.

The application of the Sun as a bright light source for the solar occultation technique (Fig. 2) determined the field of view (FOV) of the instrument. It constrains which rays emitted from the solar disk and refracted in the Venusian atmosphere will finally enter the spectrometer and reach the detector. Because, at Venus, the Sun has an apparent diameter of 44′, the FOV in the spatial direction was limited to 30′ to prevent solar limb darkening effects. This choice is also compatible with observing the Sun (apparent diameter, 32′) during ground-based tests. For the spectral direction, perpendicular to the spatial direction, a FOV of 2′ was considered to allow for good height resolution during the inversion of the Venus

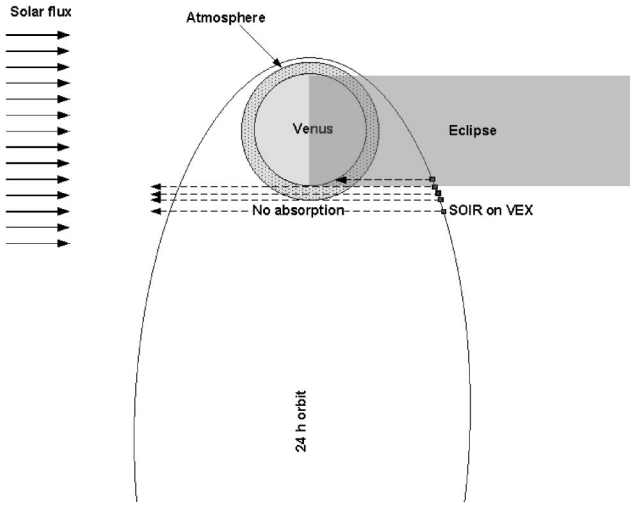

Fig. 2. Composition showing the Sun as a source, the Venusian atmosphere, and the SOIR spectrometer in orbit around Venus pointing at the Sun during a solar occultation.

occultation data. Hence a rectangular field of view of 2′ by 30′ was defined. It is our aim to control the attitude of the VEX spacecraft during an occultation observation such that the bore sight of the SOIR instrument is pointing to the Sun and that the long side of the rectangular FOV remains parallel to the planet's limb.

Because SOIR had to be put on top of the already existing SPICAM-L part of the SPICAV experiment, the mass available for SOIR was limited to 6.5 kg and its volume to 414 mm by 254 mm by 210 mm. In addition, for thermal reasons the spectrometer's entrance aperture and the corresponding aperture in the satellite wall had to be on a specific side (+Y) of the spacecraft and were restricted in diameter. Therefore a periscopelike device had to be added to the sidewall of the instrument (visible in Figs. 1 and 10 below) because the VEX solar viewing boresight was at an angle of 60° with respect to the SOIR optical axis. One of the most severe design constraints was the thermal environment imposed by the satellite in operational (−20 °C to +40 °C) and nonoperational (−30 °C to +50 °C) conditions. Table 1 summarizes the spectrometer design objectives.

4. Spectrometer Design

The main drivers for SOIR design were the available solar input, the imposed maximum entrance aperture diameter, the signal-to-noise ratio, the desired FOV, the desired spectral sampling interval, the desired ILP, the pixel size, and finally the acceptance angle of the AOTF.

It was decided to construct the spectrometer by using an echelle grating as a diffracting device; this grating type is known to yield high reciprocal dispersion and high throughput in a compact design. Since an echelle, like all gratings, is generating overlapping orders, an order-sorting filter, in this case a tunable

Table 1. Summary of Spectrometer Design Objectives

Characteristic	Value or Range	Unit
Wavelength range	2.32–4.25	μm
Wavenumber range	2353–4310	cm^{-1}
Spectral sampling interval	0.1	cm^{-1}/pixel
ILP	2 (FWHM)	pixels
Resolving power	23,200–43,100	$\lambda/\Delta\lambda = \upsilon/\Delta\upsilon$
Spectral field of view	2	arc min
Spatial field of view	30	arc min
Entrance aperture diameter	20	mm
Mass	6.5	kg
Dimensions (without periscope)	$414 \times 254 \times 210$	mm^3

bandpass filter, was required. Compared with orthogonal cross-dispersion solutions that use prisms or low-dispersion gratings, this technique permits the imaging of longer spectral lines on the detector and hence a larger binning factor along the lines, which results in higher signal-to-noise ratios. In the SOIR the bandpass filter is an AOTF. It has the advantages both of avoiding mechanical moving mechanisms and of quick random access to any grating order by electronic control. Moreover, by deactivating the AOTF, one can stop all solar input to the spectrometer; this allows a thermal background spectrum to be measured that can be subtracted from the observed spectrum. Figure 3 represents a simplified two-dimensional setup of a compact high-resolution spectrometer that uses an AOTF–echelle combination.

The spectrometer is composed of three main parts: (a) the front end part, which collects the solar light, defines the FOV, and restricts the observed wavelength domain; (b) the spectrometer itself, which determines the free spectral range (FSR) and the ILP, and finally (c) the detector system that records the spectra according to a spectral sampling interval.

The front end starts at the AOTF entrance optics (1; Fig. 3) that reduce the diameter of the incoming light beam such that it becomes compatible with the AOTF acceptance aperture. In the intermediate image plane of the entrance optics a first diaphragm (2) is placed that limits the FOV to slightly larger than the desired FOV. Then the beam enters the AOTF (3) to filter out unwanted orders. When it is activated with a RF signal, the AOTF directs the small fraction of the beam that corresponds to the wavelength domain to be analyzed along its optical axis. The AOTF exit optics (4) images the beam onto the spectrometer entrance slit (5), which is the entrance aperture for the spectrometer part of the instrument. A collimating lens (6) captures the light passing through the spectrometer entrance slit and collimates and transports it as a parallel beam to the dispersing element (7), i.e., the echelle grating located between collimator lens and imaging lens. Finally, the light diffracted by the grating is imaged via a camera lens (8) onto the detector (9).

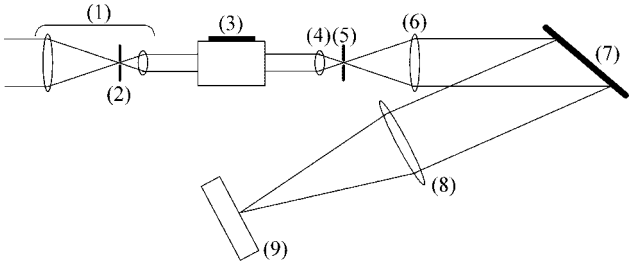

Fig. 3. Simplified two-dimensional optics schematic of the SOIR spectrometer.

To obtain a compact optical scheme for the high-resolution spectrometer part, a quasi-Littrow configuration was selected, in which the functions of the collimation lens and of the imaging lens are merged into a single off-axis parabolic mirror. An additional benefit is that no coalignment of two separate lenses is needed. Figure 4 depicts the detailed optical scheme and the associated ray tracing that is described below. The main recognizable optical units are (1) the entrance optics, (2) the diaphragm, (3) the AOTF, (4) the AOTF exit optics, (5) the spectrometer slit, (6) the off-axis parabolic mirror, (7) the echelle grating, (8) the folding mirror, (9) the detector optics, and finally (10) the detector.

5. Imager's Focal Length and Spectral Sampling Interval

The focal length of the imaging mirror in the spectrometer, together with the angular dispersion of the echelle grating and the pixel size of the IR detector, defines the spectral sampling interval (SSI) of the system. As the SSI is imposed (Table 1), the required focal length of the imaging lens can be derived.

The angular dispersion[20] D of a nontilted echelle grating at the Littrow condition is given by

$$D = \frac{2 \times \tan \theta}{\lambda}, \tag{1}$$

where D, λ, and θ are the angular dispersion in radians per wavelength unit, the wavelength, and the blaze angle of the echelle.

The SSI,[20] expressed in wavelength units per pixel, is then given by

$$\mathrm{SSI} = \frac{p}{f_{\mathrm{imager}}} \times \frac{1}{D} = \frac{p \times \lambda}{f_{\mathrm{imager}} \times 2 \times \tan \theta}, \tag{2}$$

and the derived focal length by

$$f_{\mathrm{imager}} = \frac{p \times \lambda}{\mathrm{SSI} \times 2 \times \tan \theta}, \tag{3}$$

where p and f_{imager} are the detector pixel size and the focal length of the imaging mirror. When the SSI is expressed in wavenumber units per pixel, Eq. (3)

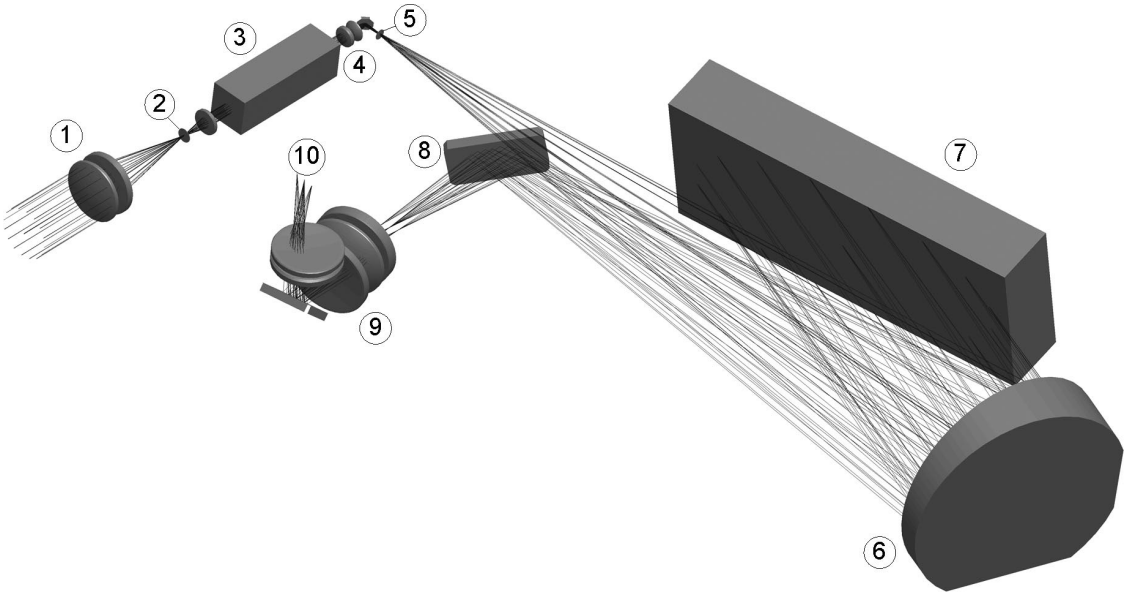

Fig. 4. Three-dimensional representation of the main SOIR optics elements and ray tracing.

becomes

$$f_{\text{imager}} = \frac{p}{\text{SSI} \times \lambda \times 2 \times \tan\theta}. \quad (4)$$

It is clear that the focal length computed for a given grating blaze angle and detector pixel size, and for a desired spectral sampling interval expressed in wavenumbers, depends inversely on the wavelength. Knowing the specified SSI (0.1 cm^{-1}) over the whole wavelength range, the pixel size (30 μm), and the blaze angle of the grating [63.43° or arctan(2)], one can find the derived imager focal lengths, 323 mm at 2.325 μm and 177 mm at 4.25 μm. As the optical design had to fit the available volume, a compromise value of 300 mm was adapted for the focal length, thus fulfilling the SSI requirement for wavelengths of 2.5–4.25 μm, with a slight deviation at 2.325–2.5 μm.

6. Echelle Free Spectral Range and Acousto-Optic Tunable Filter Characteristics

As demonstrated by formula (5), the FSR[20] of the echelle grating, the range of wavelengths in which there is no interference or superposition by light from adjacent orders, is independent of wavelength when it is expressed in wavenumber units:

$$\text{FSR} = \Delta\upsilon_{\text{free}} = \frac{1}{2 \times d \times \sin\theta \times \cos\varphi}, \quad (5)$$

where d represents the groove step, θ the blaze angle, and φ the tilting angle of the echelle. As the FWHM AOTF bandwidth, expressed in wavenumber units, is almost constant over the complete wavelength range, the FSR of the echelle and the AOTF bandwidth can be matched. For a groove step of 250 μm, a blaze angle θ of arctan 2, and a tilting angle φ of 2.6°, the echelle's FSR equals 22.38 cm^{-1}, which corresponds to an AOTF bandwidth that can be achieved with state-of-the art technology.

The AOTF used in this instrument was custom designed and manufactured in Russia by AFAR, NPO SPURT (Zelenograd, Moscow region) according to the specifications stated in Table 2. The actual IR AOTF device consists of a birefringent TeO_2 (paratellurite) tetragonal crystal (group 422) that is transparent in the spectral range 0.35–5 μm. AOTFs made of this material as well as their design have been described extensively in the literature.[21]

SOIR AOTF is employed in the classical noncollinear large-aperture configuration[22] in which a nonpolarized incident light beam produces two beams with different polarizations that are diffracted at a small angle with respect to the undiffracted output beams. In the SOIR we use only the ordinary polarization of the incoming radiation, (perpendicular to the drawing

Table 2. Specified AOTF Characteristics

Characteristic	Value or Range	Unit
Material	TeO_2	
Wavelength range	2.325–4.25	μm
Spectral bandwidth (FWHM)	≤22	cm^{-1}
Acceptance aperture in plane of diffraction	>10	mm
Acceptance aperture ⊥ to plane of diffraction	>4	mm
Acceptance angle in plane of diffraction	±2	°
Acceptance angle ⊥ to plane of diffraction	±3	°
Diffraction angle	4.6	°
AOTF radio frequency	13.5–25	MHz

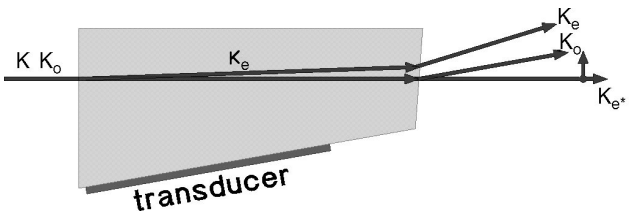

Fig. 5. SOIR AOTF: Incoming ordinary (k_o) and extraordinary (k_e) beams and outgoing useful diffracted extraordinary beam (k_e*).

plane in Fig. 5) to keep the design simple. At the AOTF output the polarization of the diffracted beam changes to extraordinary. The deflection angle of the diffracted beam, because of Bragg diffraction by the periodic acoustic wave combined with rotation of the polarization plane, is only weakly dependent on wavelength. This dependency is compensated for by the inclined output facet of the AOTF (4.2° in Fig. 6). This oblique cut also refolds the diffracted output beam such that it remains nearly collinear with the incoming beam. The strong undiffracted beam exits the crystal at an angle of 4.6° and can therefore in a easy way be separated from the useful output beam.

The central wavelength of the AOTF bandpass is inversely proportional to the frequency of the applied acoustic wave interacting with the optical waves. The acoustic wave is injected into the crystal by means of a transducer that is converting an electrical rf wave into acoustic power. The rf generator, which generates the rf wave, is itself driven by a small-signal rf carrier produced in SOIR electronics. Both frequency and amplitude can be electrically tuned at random.

The power consumed by an AOTF operating at long IR wavelengths is a potential problem. It not only affects the power budget and the thermal regime of the whole instrument, but internal thermal dissipation directly influences the tuning and bandpass characteristics of the AOTF. To minimize required rf power, the acousto-optic interaction length should be made as large as possible. This length is constrained by the availability of big pure TeO_2 crystals: When 36 mm was the maximum that could be achieved, an AOTF configuration as shown in Fig. 6 was imposed.

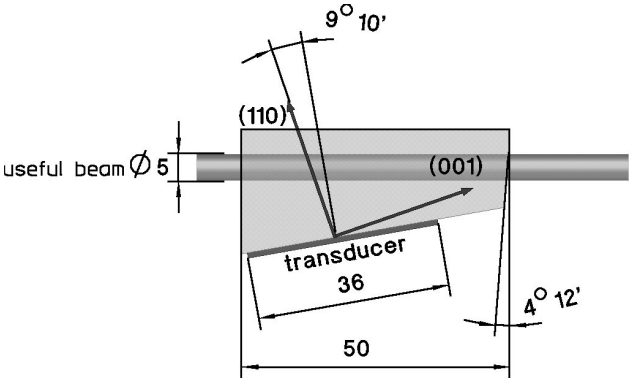

Fig. 6. SOIR AOTF configuration with orientation of the crystal axes. Dimensions in millimeters.

7. Orders and Wavenumber Ranges

As the grating groove step and the focal length of the imaging mirror are determined, the wavelength falling on the SOIR detector's central column (λ_c) as well as the wavelengths falling on the edge columns of the detector in the spectral direction (λ_e) can be computed[20] by means of formulas (6) and (7) for each order m:

$$\lambda_c \times m = 2 \times d \times \sin\theta \times \cos i \times \cos\alpha, \quad (6)$$

$$\lambda_e \times m = d[\sin(\theta + i) + \sin(\theta - i \pm \Delta\varphi)]\cos\alpha. \quad (7)$$

Here d represents the groove step of the echelle, θ the blaze angle, i the angle between the incident ray and the echelle facet normal lying in the plane that is perpendicular to the grooves and contains the echelle normal, α the angle between the incident ray and this plane, and $\Delta\varphi$ the angle between the optical axis and an edge of the detector-sensitive area. It is clear that the product (order $\times$ wavelength) remains constant for the detector's central and edge columns; hence there is a linear relationship between the wavenumber associated with a pixel and the order number.

Table 3 summarizes the wavenumbers associated with detector pixels 0 and 319 for echelle orders 101 to 194, computed with formulas (6) and (7) and corrected to take into account a small deviation from the ideal Littrow condition and a small asymmetric distortion in the spectrometer optics. This leads to 94 small wavenumber domains covering the range 2256 to 4369 cm^{-1}. For orders 101 to 122, the detector width expressed in wavenumbers is smaller than the echelle's FSR (22.38 cm^{-1}), and hence the detector will miss part of the spectrum. For orders 123 to 194 the inverse happens: The detector's width becomes equal to or larger than the FSR, and only part of the detector will be covered by the order selected by the AOTF.

8. Echelle Grating Specifications and Manufacturing

The construction of an echelle grating that has a groove density of 4 grooves/mm (groove step, 250 μm) and an effective surface of at least 60 mm by 134 mm is not evident. Bach Research Corporation, Boulder, Colorado, managed to manufacture an echelle based on the confined specifications collected in Table 4, of which the very low groove density was perhaps the most challenging.

There are two major difficulties in achieving these types of coarse echelle gratings[23]: (a) the high degree of echelle groove pitch accuracy that is required to get a usable wavefront in a high diffraction order, which is difficult to achieve during fabrication because of the high tool load and the accompanying elastic deflections experienced, and (b) a high echelle efficiency, which means an optically flat and smooth wide groove facet with respect to wavelength.

Based on its experience in both ruling and machining echelles and echelons and given the required tolerances, which were approximately 2 times tighter than previously attempted, Bach Research opted for machining the echelle on a new diamond-machining

Table 3. Computed Wavenumbers (cm^{-1}) Associated with Detector Pixels 0 and 319 for Echelle Orders 101 to 194

Order	υ_0	υ_{319}	Order	υ_0	υ_{319}	Order	υ_0	υ_{319}
101	2256.41	2274.75	133	2971.32	2995.42	165	3686.22	3716.11
102	2278.75	2297.27	134	2993.67	3017.95	166	3708.56	3738.63
103	2301.09	2319.79	135	3016.01	3040.47	167	3730.90	3761.15
104	2323.43	2342.31	136	3038.35	3062.99	168	3753.24	3783.67
105	2345.78	2364.83	137	3060.69	3085.51	169	3775.58	3806.19
106	2368.12	2387.35	138	3083.03	3108.03	170	3797.92	3828.71
107	2390.46	2409.87	139	3105.37	3130.55	171	3820.26	3851.23
108	2412.80	2432.39	140	3127.71	3153.07	172	3842.60	3873.76
109	2435.14	2454.92	141	3150.05	3175.59	173	3864.93	3896.28
110	2457.48	2477.44	142	3172.39	3198.12	174	3887.27	3918.80
111	2479.82	2499.96	143	3194.73	3220.64	175	3909.61	3941.32
112	2502.16	2522.48	144	3217.07	3243.16	176	3931.95	3963.84
113	2524.51	2545.00	145	3239.41	3265.68	177	3954.29	3986.36
114	2546.85	2567.52	146	3261.75	3288.20	178	3976.63	4008.88
115	2569.19	2590.04	147	3284.09	3310.72	179	3998.97	4031.41
116	2591.53	2612.56	148	3306.43	3333.24	180	4021.31	4053.93
117	2613.87	2635.08	149	3328.77	3355.76	181	4043.65	4076.45
118	2636.21	2657.61	150	3351.11	3378.29	182	4065.99	4098.97
119	2658.55	2680.13	151	3373.45	3400.81	183	4088.33	4121.49
120	2680.89	2702.65	152	3395.79	3423.33	184	4110.67	4144.01
121	2703.23	2725.17	153	3418.13	3445.85	185	4133.01	4166.54
122	2725.58	2747.69	154	3440.47	3468.37	186	4155.35	4189.06
123	2747.92	2770.21	155	3462.82	3490.89	187	4177.69	4211.58
124	2770.26	2792.73	156	3485.16	3513.41	188	4200.03	4234.10
125	2792.60	2815.25	157	3507.50	3535.93	189	4222.37	4256.62
126	2814.94	2837.78	158	3529.84	3558.46	190	4244.71	4279.14
127	2837.28	2860.30	159	3552.18	3580.98	191	4267.04	4301.67
128	2859.62	2882.82	160	3574.52	3603.50	192	4289.38	4324.19
129	2881.96	2905.34	161	3596.86	3626.02	193	4311.72	4346.71
130	2904.30	2927.86	162	3619.20	3648.54	194	4334.06	4369.23
131	2926.64	2950.38	163	3641.54	3671.06			
132	2948.98	2972.90	164	3663.88	3693.58			

engine built around the base of a Moore #3 measuring machine. The substrate in which the echelle was machined is a 150 mm by 60 mm by 25 mm block of aluminum 6061-T6 alloy. On the side and back of the substrate, Bach Research diamond turned a set of 30 mm by 30 mm reference mirrors to facilitate the alignment of the echelle in the spectrometer and during manufacturing. Their wavefront quality was $\sim\lambda/4$ at 632.8 nm.

Table 4. Comparison of Specified and Obtained Echelle Parameters[a]

Characteristic	Specified Value	Obtained Value	Unit
Wavelength range	2–4.2		μm
Diffraction orders	100–200		
Blaze angle	arctan(2)	63.20	degrees
Groove density	4		per mm
Groove spacing	250		μm
Total number of steps	560		
Structure width	150	150.03	mm
Groove length	60	59.94	mm
Structure thickness	25	24.99	mm
Temperature range	−50–+50		°C

[a]Material, aluminum 6061-T6; coating material, gold.

Several corrections were made to the engine, and the process of cut-and-try was repeated a number of times until the echelle ghost intensities were reduced to the order of 0.2% of the parent line. Each machined echelle was tested for ghosts and efficiency, at both 1.1 and 3.3 μm, with a 0.5 m Czerny–Turner spectrometer. Figure 7 depicts a typical ghost trace of a good echelle, measured in the IR domain in the 130th order of a 3.3 μm He–Ne laser.

Expression (8), derived by Rowland in the 19th century, in which m is the order of the parent line, ε is the amplitude of the periodic error, and d is the grating pitch, relates the first-order ghost intensity to that of the parent line for the Littrow condition:

$$\frac{I_{\text{ghost}}}{I_{\text{parent}}} = \left(\frac{m \times \varepsilon \times \pi}{d}\right)^2. \tag{8}$$

The measured peak ratio of 0.002 suggests that the amplitude of the periodic error on a groove pitch of 250 μm was reduced to ~27 nm. The SOIR echelle was also tested with visible light by use of an ADE phase shift MiniFIZ surface mapping Fizeau interferometer and was found to have a wavefront quality of approximately 0.7 wave rms in the 702nd order of

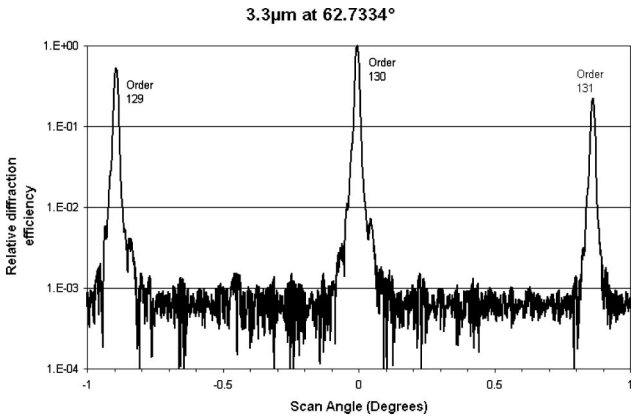

Fig. 7. Echelle grating diffraction pattern measured with a monochromatic source at 3.39 μm. Orders 129, 130, and 131 are shown.

632.8 nm laser light. The nonperiodic groove pitch error[24] can be estimated from these wavefront data by Eq. (9), wherein δx is the error in groove placement, # is the inverse of the wavefront error, $\lambda/\#$ is the fractional wavefront error, and θ is the angle of use. In a Littrow mounting condition the equation can be reexpressed in terms of groove pitch d and order of use m:

$$\delta x = \frac{\lambda/\#}{2 \times \sin(\theta)} = \frac{d}{m \times \#}. \tag{9}$$

Formula (9) yields an estimated nonperiodic placement error of 249 nm.

9. Instrument's Field of View, Entrance Optics, and Relay Optics

Inasmuch as the spectral FOV of 2′ must be imaged on two detector pixels (2 μm × 30 μm) to fulfill the Nyquist sampling criterion, the overall focal length of the spectrometer must be equal to 103 mm. The specified spatial FOV (30′) will then obviously be imaged on 30 detector pixels.

The allowed acceptance angle of the AOTF and the available entrance aperture, however, directly determine the magnification of the entrance optics in front of the AOTF. Given the entrance pupil diameter of 20 mm and the AOTF acceptance aperture (10 mm × 4 mm), a magnification factor of 5 is required.

The entrance optics consists of a telescope composed of an objective lens (Si–Ge doublet, focal length 58.4 mm) followed by a collimating lens (ZnSe singlet, focal length 11.6 mm). A refracting lens design was preferred to reflecting optics because of limited space and the specific entrance requirements. The Ge lens element also absorbs wavelengths shorter than 1.8 μm (at 300 K), stopping the UV–visible part of the solar spectrum before the AOTF. In the focal plane of the objective lens a rectangular diaphragm of 175 μm by 1250 μm with an edge thickness of 100 μm is placed that reduces the entrance optics FOV to slightly larger than the desired overall FOV. It avoids imaging the full Sun on the spectrometer slit and suppresses light scattering and ghost images in the rest of the optics; it also acts as a heat sink, since it stops a large part (70%) of the solar input flux. The entrance optics exit angle in the spatial direction (five times the desired overall spatial FOV, or 2.5°) is still well within the acceptance angle of the AOTF (Table 2).

The relay optics transports the output beam of the AOTF to the echelle grating. It consists in a telescope composed of the AOTF exit optics and the collimator formed by an off-axis parabolic mirror with a focal length of 300 mm; the latter is used 100 mm or 19° off axis and reflects the light out of the horizontal plane by 1.46°. The combined focal length of entry optics and AOTF exit optics is equal to the overall focal length (103 mm); the spectrometer itself has no effect on focal length because of its magnification factor of 1.

The magnification factor M_{AXO} of the combination of the AOTF exit optics and the collimating mirror (0.0687) is given by

$$M_{\mathrm{AXO}} = \frac{f}{f_{\mathrm{imager}} \times M_{\mathrm{AEO}}}, \tag{10}$$

in which f, f_{imager}, and M_{AEO} are the overall focal length, the focal length of the imager, and the magnification factor of the AOTF entrance optics, respectively. The spectrometer entrance slit is positioned immediately behind the AOTF exit optics at the intermediate image plane. As the slit is imaged one to one on the detector, the slit dimensions have been defined as 2 pixels wide (60 μm) by 30 pixels high (900 μm). The thickness of the slit material is 100 μm.

The maximum entrance aperture diameter D_{EA} (20 mm) is imposed by the VEX spacecraft design and has a direct effect on the Fraunhofer diffraction-limited spot size (Airy disk) on the detector. This spot diameter a, given by Eq. (11) below, increases linearly with wavelength λ, but at the largest specified wavelength (4.25 μm) it remains still smaller than the specified ILP:

$$a = 2.44 \times \lambda \times \frac{f}{D_{\mathrm{EA}}}. \tag{11}$$

10. Infrared Detector and Associated Optics

The SOIR detector assembly is located beside the spectrometer section, and therefore an extra folding mirror (8 in Fig. 4) is needed to bend the optical path clockwise by 90°. Further, a lens system is positioned after the focal plane of the spectrometer, imaging the entrance aperture of the spectrometer onto the cold shield aperture of the cooled IR detector and projecting the slit image, formed by the collimating–imaging mirror, on the detector with a magnification of 1×. The system contains five spherical lenses and compensates for aberrations created by the off-axis parabolic mirror. The first and the fourth lenses are made of Ge, the third and the fifth of Si, and the second of ZnSe. A mirror between the third and the fourth lenses bends the light

Table 5. Main Electro-Optical Characteristics of the Customized SOFRADIR ID MM0067 Detector[a]

Characteristic	Value	Unit
Number of pixel rows	256	
Number of pixels per row	320	
Cold shield aperture	$f/4$	
Integration capacitor for gain setting 0/1	0.7/2.1	pF
Maximum charge for gain setting 0/1	12/37	10^6 e^-
Video output range	1.6–4.4	V
Video dynamic range	2.8	V
Minimum integration time	3	μs
Standard wavelength range	3.7–4.8	μm
Customized cut-on at 70% of maximum	1.8	μm
Customized cutoff at 70% of maximum	4.2	μm
Typical quantum efficiency at 3.5 μm	0.75	e^-/photon
Read-out speed for single video output	1–6	MHz
Typical focal plane temperature	≤110	K

[a]Typical relative spectral pixel response, see Fig. 8.

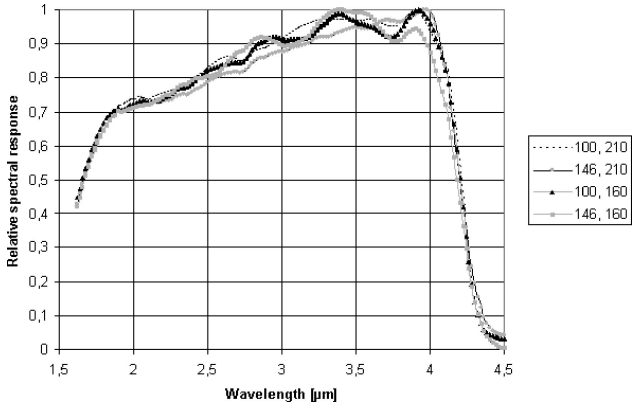

Fig. 8. Relative spectral response of the customized SOFRADIR ID MM0067 IDDCA detector. Curves for four pixel locations.

path upward by 90°. The final image of the spectral lines on the detector makes a slight angle with respect to the optical axis of the entrance optics, and therefore the whole detector assembly is rotated by 2.45° clockwise about an axis perpendicular to the spectrometer's base plate.

The detector system itself is a slightly modified standard integrated detector Dewar cooler assembly of type ID MM0067 manufactured by SOFRADIR, Chatenay-Malabry, France. The main characteristics of this customized version are summarized in Table 5. It includes a high-sensitivity focal plane array (FPA) that comprises a two-dimensional detector array made of photovoltaic mercury cadmium telluride [HgCdTe (MCT)] pixels of 30 μm by 30 μm that are organized as 320 columns by 256 rows. The sensitive area of 9600 μm by 7680 μm has a fill factor greater than 90%. All pixels are connected by means of indium bumps to a complementary metal-oxide detector readout integrated circuit that forms a sandwich with the MCT array. The readout integrated circuit reads the charge from each MCT photovoltaic diode by direct injection and integrates it on the pixel's input capacitor (selectable 0.7 or 2.1 pF) during a programmable integration time. We have opted for reasons of power, commanding, and simplicity to read out only a programmable window (8 rows of 320 pixels) of the FPA in the single output mode at a 1 MHz rate. As a consequence of the direct injection readout method, the linearity of the detector is not constant over the whole video output range. However, a linearity of 95% can be obtained when the integrated charge is 7% to 97% of the pixel's saturation value. In this application, in which we observe solar occultation spectra, the integration time is to be chosen such that the detector signal stays within this range. Absorption peaks that do not descend below 50% of saturation will be measured with a linearity of 99%.

The detector FPA is mounted in an evacuated Dewar with a customized optical Si window (relative spectral response in Fig. 8) and is surrounded with a cold shield with an $f/4$ aperture. It is cooled by a closed cycle miniature Stirling cooling machine (RICOR, Israel) that was adapted for space applications. SOFRADIR manufactured the FPA and integrated it with the Dewar and the cooler; the BIRA-IASB developed a proprietary space-qualified cooler motor control circuit (see below).

11. Detector Readout and System Control Electronics

The SOIR spectrometer is controlled by a dedicated space-qualified electronics unit, a simplified block diagram of which is shown in Fig. 9. The central part of the electronics is the central control and communications board, which contains a field programmable gate array that performs five main tasks: (1) reception and analysis of telecommands and production of telemetry data issued by or sent to the spacecraft; (2) command of the housekeeping board (HSK, Fig. 9) measuring essential housekeeping data, such as temperatures of optical parts and supply voltages; (3) generation of clock signals required for the readout of the FPA, the analog video signal of which is amplified, sampled, and converted to digital on the video sampling proximity electronics board; (4) generation by means of a direct digital synthesizer of the 32 bit wide digital code representing the tunable rf sine waveform for the AOTF; (5) control with an embedded proportional-integral-derivative controller program of the RICOR cooler temperature. The digital rf code generated on the central control and communication board is used by the rf generator board, which produces the rf analog signal for the AOTF. The RICOR cooler control board receives optocoupled digital motor control signals from the central control and communication board and regulates the detector

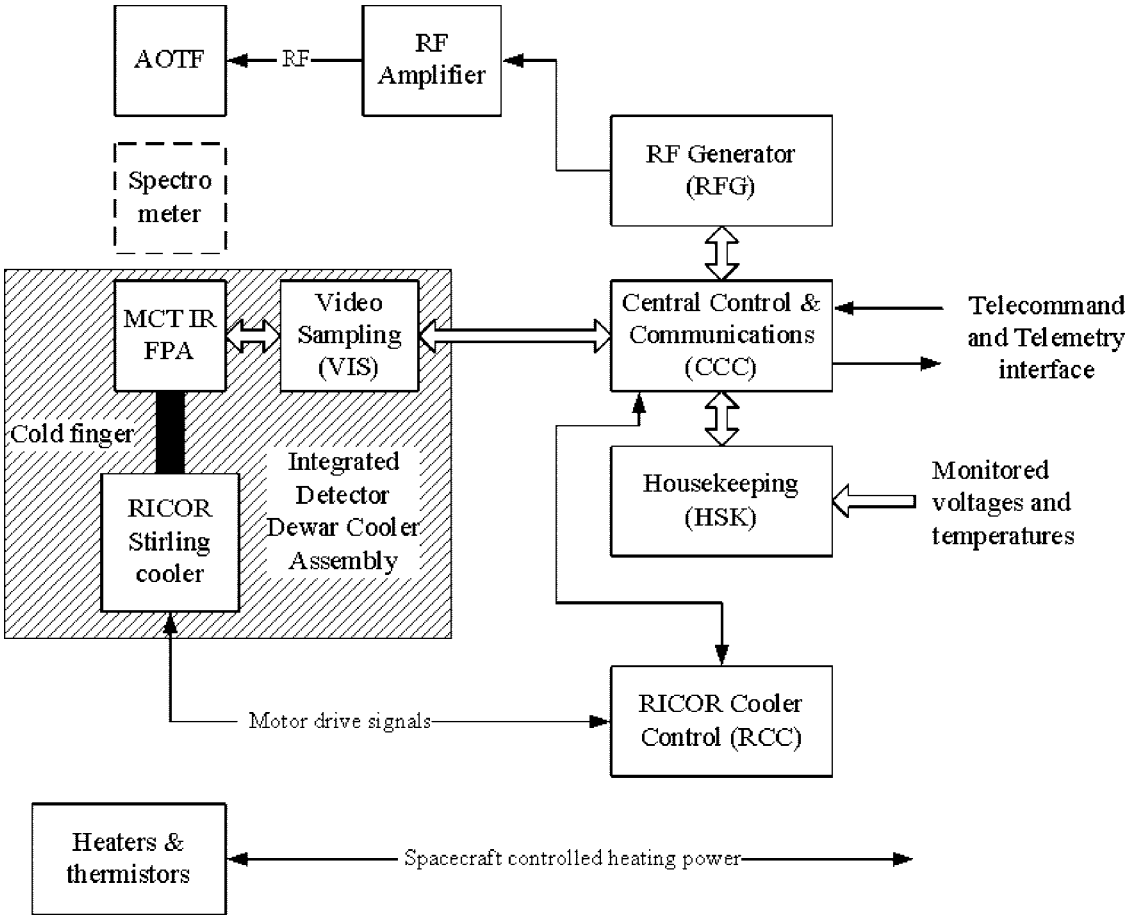

Fig. 9. Simplified block diagram of the SOIR control electronics. Power converters and power switching not shown.

cooler temperature by means of pulse width modulation.

One of the nice features of the spectrometer's control electronics is that, because of its fast rf on–off switching capabilities, the AOTF order-sorting filter can be used to make two successive measurements of the same spectrum: one with signal plus thermal background and one with thermal background alone.

12. SOIR Observation Modes

Before a solar occultation observation is started and the detector's FPA supply voltages are activated, the instrument goes into a precooling phase during which the FPA's temperature is decreased to its nominal operating temperature (approximately 90–100 K); during this phase, only housekeeping data are sent through telemetry. The parameters required for the precooling phase are sent in a first type of telecommand packet and contain settings such as the precooling duration, the desired FPA temperature, and the cooling control loop coefficients. At the end of precooling the spectrometer expects a second type of telecommand packet containing the observation settings for the occultation. The observation itself consists in the continuous recording and sending of spectra at a rate of 1 spectrum/s (rate imposed by spacecraft telemetry resources); this process continues until instrument switch-off.

Different types of observation schemes, all working at the imposed rate, may be executed. The standard observation condition during solar occultations comprises the repeated readout of the spectrum that corresponds to a fixed grating order selected by the AOTF frequency setting and hence to a fixed wavenumber range. This scheme may be extended by allowing as many as 4 AOTF frequency hops within each sampling period of 1 s, permitting the recording of a sequence of 1–4 different wavelength bands. This is applicable only if the sum of all required detector integration times and AOTF settling times does not exceed the sampling period (1 s). The essential parameters related to the programming of this scenario are the exact position of the spectral window on the detector, the number of pixels along the spectral lines and their binning factor (1, 2, 4, 8, 16, or 32), the number of different spectral domains per sampling period (1–4), and the 4 possible parameter sets associated with these domains (FPA integration time, number of times a spectrum can be accumulated during one sampling period, the AOTF frequency, and power setting). An additional parameter flag allows subtracting a background spectrum measured imme-

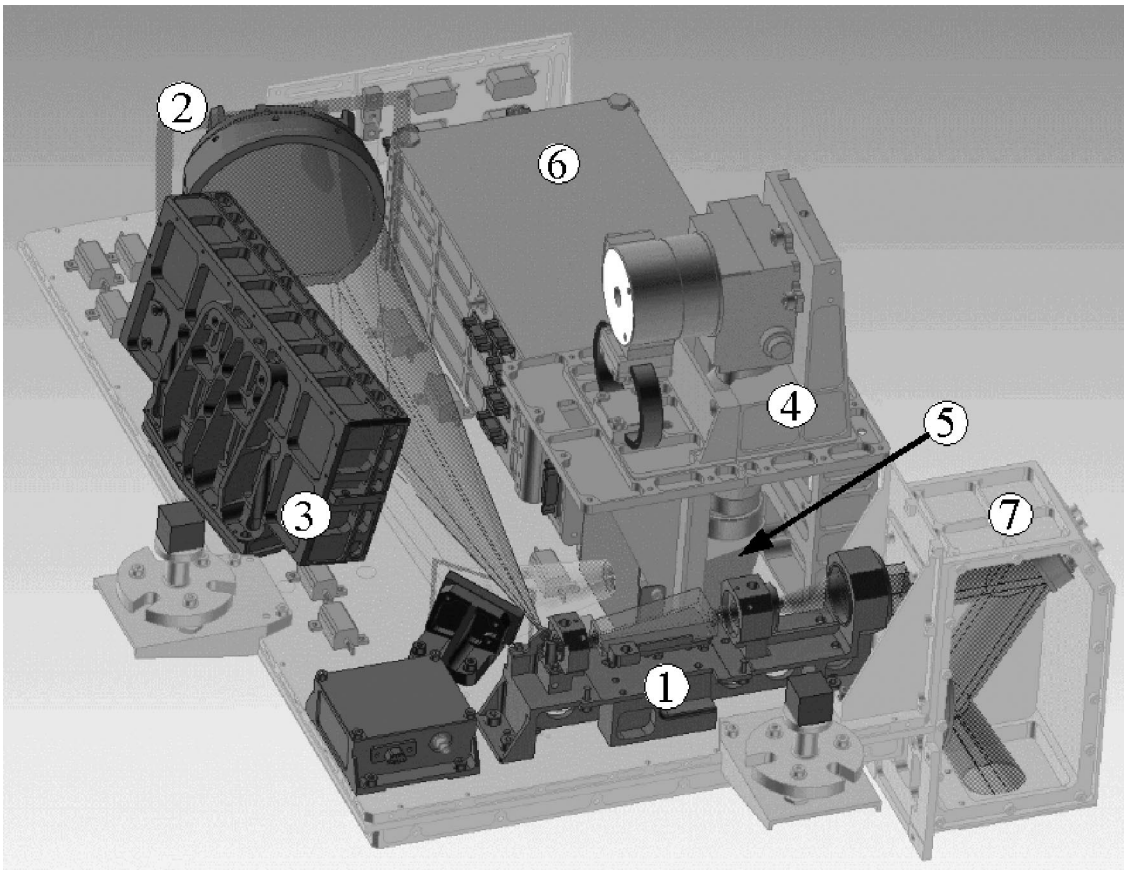

Fig. 10. SOIR mechanical structure in three dimensions.

diately before each signal spectrum; in this case, 1–4 measurement pairs (signal, background) can be recorded per sampling interval.

A different scenario, called automatic detector window stepping, can be used for a complete readout of the focal plane image at a fixed AOTF frequency. At each sampling period the next detector window (8 rows of 320 pixels) is accessed and read out. In total, 32 sampling periods are required for reading out the complete detector array once. This scenario is useful during the commissioning phase of the spacecraft and of the SOIR to derive detector and spectrometer characteristics.

A last built-in scenario is echelle order stepping. During each sampling period the AOTF frequency is increased by a constant but programmable increment, thus permitting an AOTF frequency scan from a minimum to a maximum frequency. If the minimum frequency and the frequency increment are programmed such that for each step the AOTF bandpass is positioned in the center of the detector window, then we can organize a perfect spectrum scan of succeeding orders. It is obvious that this scenario allows recording scans over the complete wavelength domain, hence from 2.2 μm (order 194) to 4.3 (order 101), to be made. This property can be used during instrument commissioning in cruise phase and in orbit around Venus outside eclipses to get a reference observation of the solar spectrum, permitting the assessment of the optimum integration time settings for solar observations and a calibration of the wavenumber range.

13. Mechanical Structure and Optical Alignment

Because it had to be installed on an internal panel of the VEX spacecraft and on top of an existing instrument that was originally conceived for the MEX mission (SPICAM-L), the surface of the SOIR's baseplate was confined to 414 mm length by 254 mm width. This baseplate, which carries the holders of the individual optical parts, the electronic boards, and the cabling, forms the mechanical interface with the SPICAM-L. Its design is a compromise between low mass and stiffness; its overall thickness is 24.6 mm, and it has a flat-topped surface and a rib structured bottom.

The main mechanical subunits depicted in Fig. 10 are (1) the AOTF bridge carrying the AOTF and its entrance and exit optics, a small folding mirror, and the spectrometer's entrance slit, (2) a holder plus a baffle for the parabolic mirror, (3) a boxlike grating holder providing the necessary tilting of the echelle grating, (4) a support structure for the detector unit, (5) a detector entrance optics holder, and (6) a number of boxes containing the electronic boards and providing radiation shielding. All structural elements, including the baseplate, are made of AISI 7075 space-qualified aluminum. Some elements, such as the folding mirror

Table 6. Estimated Thermal Background and Fraction of Pixel Saturation

	Temperature (K)						
Units	313	303	293	283	273	263	253
10^5 e^- $pixel^{-1}$ ms^{-1}	2.82	1.91	1.26	0.809	0.504	0.303	0.176
% of pixel saturation (ms^{-1})	2.23	1.52	1	0.64	0.4	0.24	0.14

holder and the AOTF support, are manufactured in stainless steel for a better compatibility among optical element, appropriate space-qualified glue, and structure and hence a better resistance to vibrations or shocks. To prevent light scattering and for thermal reasons all structural elements in or in the neighborhood of the optical path are surface treated by space-qualified optically black anodization.

The height of SOIR's main cover is 100 mm, which is locally reduced to 70 mm to fit underneath a VEX subsystem and extended to 210 mm at the location of the detector. It protects the delicate optical parts inside the instrument, contributes to the overall stiffness, provides additional shielding against radiation, and serves as a support for the thermal multilayer insulation blanket, which covers the whole of SOIR.

The completely integrated SPICAV instrument has been successfully qualified during mechanical vibration tests. Furthermore, all SOIR subassemblies, as well as the fully integrated SOIR and SPICAV instruments, have passed several thermal-vacuum tests in an operational temperature range of −40 °C to +50 °C and in a nonoperational range of −40 °C to +60 °C.

The optical axis of the entrance optics is situated 45 mm above the baseplate. In the plane parallel to the baseplate it can be aligned to 1′ with respect to the mechanical structure, and by design it is parallel within 20′ to the baseplate. SOIR is a Sun-pointing instrument designed for observations that use the solar occultation technique (Fig. 2). However, the optical axis of SOIR and the solar port of the VEX do not coincide, and therefore a two-mirror periscope [(7) in Fig. 10] is added externally at the entrance of the instrument. It folds the solar light beam, which passes through an aperture in the spacecraft's side wall at an angle (60°) with respect to the instrument's baseplate, into SOIR. One of the periscope mirrors is adjustable in three axes, allowing for perfect alignment between the desired inclined line of sight and the SOIR's optical axis; an external cube mounted at the outside of the baseplate is used as a reference.

14. Thermal Environment

From an optical design point of view, the ideal operating temperature range for SOIR is −5 °C to +20 °C; lower temperatures lead to lower thermal background. The instrument is thermally coupled to neighboring instruments and satellite subsystems in three ways: by radiative heat exchange via a 12 layer thermal blanket (multilayer insulation), by conduction by means of its own baseplate and SPICAM-L to a thermal reference point on the spacecraft, and finally by conduction by means of a flexible multilayer cupper thermal strap directly from its baseplate to a second thermal reference point that is connected to a cold spacecraft wall. The temperatures of both thermal reference points are independently regulated by the spacecraft. Other heat sources and sinks are the internally dissipated power (17 W during the detector precooling phase and 16 W in the measuring phase), the solar flux absorbed in the entrance optics during Sun-pointing periods, and heat loss to deep space through the open periscope. In cold nonoperational cases, additional heating for SOIR's baseplate is provided by means of two redundant series of heating elements that are switched on by the satellite when the baseplate's temperature drops below −5 °C and off when the temperature rises above 0 °C.

15. Thermal Background, Signal and Noise

A significant contribution to the signal measured by the detector's FPA comes from the thermal background emitted by the optical elements and the surrounding mechanical parts. To exclude the thermal radiation emitted by the latter, the detector Dewar is equipped with an $f/4$ cold shield that is imaged on SOIR's entrance aperture. The only structure that is directly in view of the FPA is the spectrometer slit mount that is in focus for the detector. It shields the FOV's limiting diaphragm mounted in the entrance optics as well as all other optical elements in front of the slit. The little thermal radiation transmitted by the slit is further dispersed by the echelle grating, and therefore each detector pixel will receive only energy emitted in a small spectral interval corresponding to the SSI. The mirrors and lenses placed between the grating and the detector will contribute a lot more, because each detector pixel will receive thermal radiation in the much wider 1.8–4.3 μm band. Table 6 represents the thermal background per pixel and per millisecond for various uniform environmental temperatures, as calculated assuming worst-case emissivities and transmission and reflection efficiencies for lenses, mirrors, parabolic mirror, echelle and slit mount, and a constant FPA quantum efficiency of 70%. These results indicate that, at the maximum expected operating temperature of SOIR (293 K), thermal background will be limited to 1% of full scale per integration time slice of 1 ms.

The noise component associated with the thermal background is one of the main noise sources for the detector; the other is the shot noise of the solar signal itself. Tables 7 and 8 represent the expected solar signal as well as the thermal and shot noise at 2.2 and

Table 7. Estimated Signal, Noise Sources, and SNR for 2.2 μm and a 36 ms Integration Time

		Temperature (K)						
Measurand	Units	313	303	293	283	273	263	253
Thermal electrons	10^6 e^-	10.2	6.87	4.54	2.91	1.81	1.09	0.632
Thermal noise	e^-	3186	2622	2130	1707	1347	1045	795
Expected signal	mW m^{-2} $pixel^{-1}$	30	30	30	30	30	30	30
Signal electrons	10^6 e^-	7.48	7.48	7.48	7.48	7.48	7.48	7.48
Shot noise	e^-	2734	2734	2734	2734	2734	2734	2734
Total noise	e^-	4199	3788	3466	3223	3048	2927	2848
SNR		1781	1974	2157	2319	2453	2554	2625

Table 8. Estimated Signal, Noise Sources and SNR for 4.3 μm and a 36 ms Integration Time

		Temperature (K)						
Measurand	Units	313	303	293	283	273	263	253
Thermal electrons	10^6 e^-	10.2	6.87	4.54	2.91	1.81	1.09	0.632
Thermal noise	e^-	3186	2622	2130	1707	1347	1045	795
Expected signal	mW m^{-2} $pixel^{-1}$	3.2	3.2	3.2	3.2	3.2	3.2	3.2
Signal electrons	10^6 e^-	1.60	1.60	1.60	1.60	1.60	1.60	1.60
Shot noise	e^-	1263	1263	1263	1263	1263	1263	1263
Total noise	e^-	3428	2910	2476	2123	1847	1639	1493
SNR		465	548	644	751	864	973	1069

4.3 μm, respectively, and for the same operating temperatures as mentioned in Table 6. For 2.2 μm the integration time for which the detector becomes just saturated by the sum of signal and thermal background equals 36 ms when the operating temperature is 293 K. For this integration time and operating temperature the estimated signal-to-noise ratio (SNR) varies from 2157 at 2.2 μm and 644 at 4.3 μm. The SNR will slightly improve if the operating temperature approaches the nominal SOIR operating temperature (273 K). It is also clear that for 4.3 μm one can double the integration time until the pixel saturates and improve the SNR by a factor of $\sqrt{2}$.

16. Predicted and Observed Optical and Spectral Performance

The ILP predicted by OIP comes very close to the specified width of 2 pixels. Figure 11 shows the calculated ILPs for three wavelengths: 2.32, 3.16, and 4.24 μm. Smile, frown, and the displacement of the spatial field have also been verified by calculation. Smile (deviation from a straight line of the slit image on the detector at one particular wavelength) will be unnoticeable because it is always less than 1/10th of a pixel, and frown (deviation from a straight line of the different images of one particular slit point for different wavelengths within one diffraction order) will never be larger than half a pixel. Finally, the displacement between the central wavelengths of different orders turns out to be less than 1/6th of a pixel.

The predicted spectral performance of the SOIR spectrometer was verified under normal lab conditions at the 3.39 μm line of a He–Ne laser. The laser output was diffused, collimated, and sent into the spectrometer's optical entrance aperture (no periscope installed). Because of the small bandwidth of the laser line, the detector's image should be a one-to-one copy of the slit. Figure 12(a) shows a gray scale representation of a two-dimensional rectangular cutout of the detector's response in the area where the slit image of 2 by 30 pixels is formed. One can also clearly observe the excellent aberration correction and the resultant straight spectral line. Figure 12(b) shows a cross section of the image along a pixel row, confirming that the ILP is as expected. One can also derive the overall noise (detector + electronics) in the detector area outside the spectral lines derived from the same measurement by looking at nonilluminated

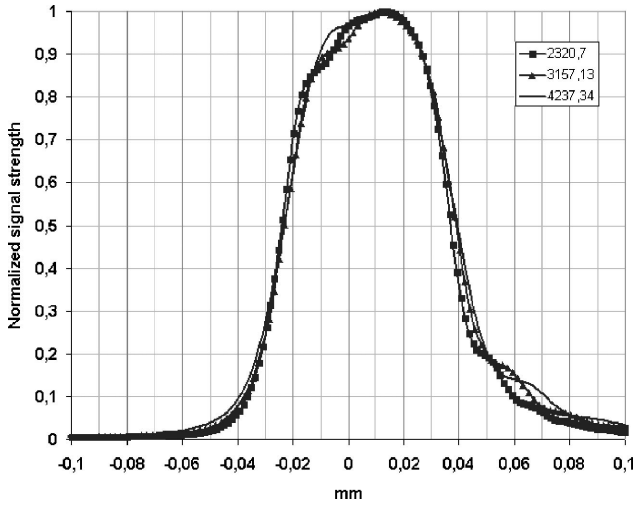

Fig. 11. Predicted ILP for three wavelengths: 2320.7, 3157.13, and 4237.34 nm.

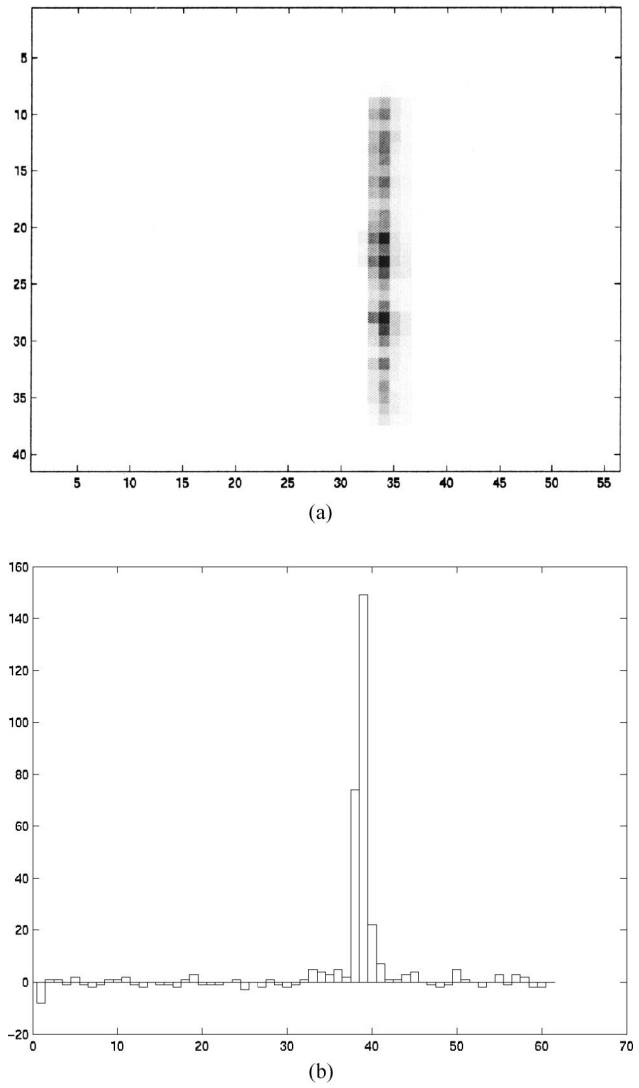

Fig. 12. Image of spectrometer slit on detector with monochromatic 3.39 μm laser source: (a) gray-scale two-dimensional image. Horizontal axis, relative pixel number along the detector row; vertical axis, relative pixel number along the detector column. (b) Image cross section along a detector row. Horizontal axis, relative pixel number along the detector row; vertical axis, detector signal in arbitrary units.

pixels; it amounts to a peak-to-peak noise of 5 least significant bits.

A more elaborate test with the Sun as a source, and applying the described echelle order stepping scenario, was also performed. Solar rays undergoing absorption by the Earth's atmosphere were reflected by a mirror outside the lab and directed along the optical axis of SOIR, which was located in a clean room. A typical readout, recorded at the same AOTF frequency used to perform the 3.39 μm (2949 cm^{-1}) laser test, is shown in Fig. 13; it shows 8 spectra obtained by applying 4-to-1 binning on 32 detector rows of 320 pixels each. The quality of the spectral lines observed during the laser test is confirmed: spectral lines remain perfectly perpendicular to the

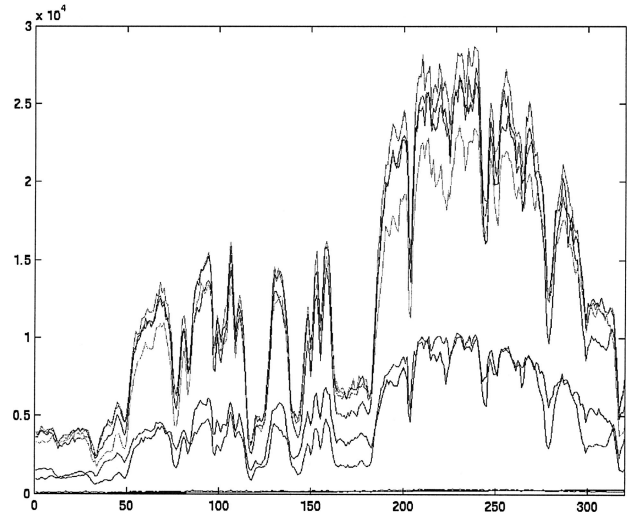

Fig. 13. Typical uncalibrated detector output recorded with the AOTF tuned to the 3.39 μm band during observation through the Earth's atmosphere. Eight spectra are shown, resulting from 32 detector rows of 320 pixels each; each spectrum obtained by 4-to-1 binning of 4 detector rows. Horizontal axis, pixel number along the detector row; vertical axis, detector signal expressed as accumulated analog-to-digital converter codes.

diffraction direction and parallel to the detector columns.

During this quick test the selected detector readout window was not in accordance with the height of the spectral lines, and the relation between the wavenumber scale and the AOTF frequency was still uncalibrated. This relation and the diffraction in the different orders can be calibrated in flight during the cruise phase by use of the solar spectrum and its known absorption lines as a reference. Nevertheless, by comparing parts of the spectrum obtained with a synthetic spectrum (Fig. 14) computed by means of the PcLnwin computer program it was demonstrated

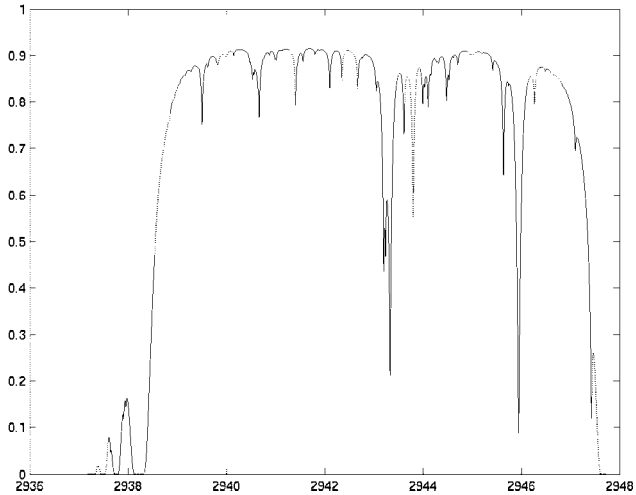

Fig. 14. CH_4 absorption spectrum for the range 2938–2948 cm^{-1} obtained by simulation assuming observation of the Sun from ground at a 45° zenith angle and through the Earth's atmosphere. Spectral resolution, 0.1 cm^{-1} HWHM.

that the spectrometer attained the projected high resolution. This program simulated an observation of the Sun from ground through the Earth's atmosphere at a 45° zenith angle with CH_4 as the absorbing molecule and for a spectral resolution of 0.1 cm^{-1} HWHM. After comparison with the synthetic spectrum (Fig. 14), the absorbing features seen at the right of Fig. 13 (pixels 180–320) can clearly be attributed to CH_4 absorbing in the 2938–2948 cm^{-1} range and their line width is as expected.

Most of the spectra recorded in a particular echelle order also show interference by neighboring diffraction orders, because the applied AOTF frequencies used were not calibrated and because the AOTF bandpass is not a square that fits exactly one order but shows a $sinc^2$ behavior giving rise to sidelobes. The noticeable feed-through effect can be corrected for by postprocessing when one knows the synthetic spectra of expected atmospheric constituents.

17. Conclusions

The high-resolution IR spectrometer described in this paper is to our knowledge the first spectrometer based on a combination of a highly dispersive echelle and an acousto-optical tunable filter to be put in space. On 9 November 2005 it was launched on board the ESA Venus Express spacecraft from the Baikonour launching site in Kazakhstan by means of a Soyuz–Fregat launcher. Insertion into an orbit around Venus was achieved on 11 April 2006, and the final operational 24 h orbit was reached on 7 May 2006.

It is obvious that the field of applications for the spectrometer described is not limited to the VEX mission only. It could be extremely useful to study the presence of methane in the Martian atmosphere by solar occultation, and this spectrometer could perform such a task with a 10-times-higher spectral resolution than is possible with present instruments in orbit around Mars.

The authors thank Jean-Loup Bertaux, principal investigator of the SPICAV experiment, for his many intensive and scientifically founded interventions at the ESA level, defending and promoting the SPICAV experiment and its extension, the SOIR high-resolution IR spectrometer. Furthermore, we express our gratitude for the financial support that we received from the Belgian Federal Science Policy Office, which completely funded the design and manufacturing of SOIR as well as part of the construction of the SPICAM-L (ESA PRODEX contract 90113) during the years 2003–2005.

Our special thanks go to the technical people at BIRA-IASB and OIP, Belgium, and the Service d'Aéronomie, France, who have made the successful assembling and testing of SOIR and the SPICAM-L and their integration into the SPICAV possible under severe time pressure.

References

1. European Space Agency, *Mars Express–The Scientific Payload,* ESA Spec. Publ. SP-1240 (European Space Agency, 2004), pp. 1–219.
2. V. Formisano, V. I. Moroz, F. Angrilli, G. Bianchini, E. Bussoletti, N. Cafaro, F. Capaccioni, M. T. Capria, P. Cerroni, G. Chionchio, L. Colangeli, A. Coradini, A. Di Lellis, S. Fonti, R. Orfei, E. Palomba, G. Piccioni, B. Saggin, A. Ekonomov, A. Grigoriev, V. Gnedykh, I. Khatuntsev, A. Kiselev, I. Matsygorin, B. Moshkin, V. Nechaev, Y. Nikolsky, D. Patsaev, A. Russakov, D. Titov, L. Zasova, M. I. Blecka, A. Jurewicz, M. Michalska, W. Novosielski, P. Orleanski, G. Arnold, H. Hirsch, H. Driesher, J. Lopez-Moreno, R. Rodrigo, J. Rodriguez-Gomez, and G. Michel, "PFS: a Fourier spectrometer for the study of Martian atmosphere," Adv. Space Res **19,** 1277–1280 (1997).
3. R. Hanel, B. Schlachman, E. Breihan, R. Bywaters, F. Chapman, M. Rhodes, D. Rodgers, and D. Vanous, "Mariner 9 Michelson interferometer," Appl. Opt. 11, **11,** 2625–2634 (1972).
4. M. R. Gunson, M. M. Abbas, M. C. Abrams, M. Allen, L. R. Brown, T. L. Brown, A. Y. Chang, A. Goldman, F. W. Irion, L. L. Lowes, E. Mahieu, G. L. Manney, H. A. Michelsen, M. J. Newchurch, C. P. Rinsland, R. J. Salawitch, G. P. Stiller, G. C. Toon, Y. L. Yung, and R. Zander, "The Atmospheric Trace Molecule Spectroscopy (ATMOS) experiment: deployment on the ATLAS space shuttle missions," Geophys. Res. Lett. **23,** 2333–2336 (1996).
5. P. F. Bernath, C. T. McElroy, M. C. Abrams, C. D. Boone, M. Butler, C. Camy-Peyret, M. Carleer, C. Clerbaux, P.-F. Coheur, R. Colin, P. DeCola, M. De Mazière, J. R. Drummond, D. Dufour, W. F. J. Evans, H. Fast, D. Fussen, K. Gilbert, D. E. Jennings, E. J. Llewellyn, R. P. Lowe, E. Mahieu, J. C. McConnell, M. McHugh, S. D. McLeod, R. Michaud, C. Midwinter, R. Nassar, F. Nichitiu, C. Nowlan, C. P. Rinsland, Y. J. Rochon, N. Rowlands, K. Semeniuk, P. Simon, R. Skelton, J. J. Sloan, M.-A. Soucy, K. Strong, P. Tremblay, D. Turnbull, K. A. Walker, I. Walkty, D. A. Wardle, V. Wehrle, R. Zander, and J. Zou, "Atmospheric Chemistry Experiment (ACE): mission overview," Geophys. Res. Lett. **32,** L15S01, doi:10.1029/2005GL022386 (2005).
6. P. Drossart, A. Semery, M. Bouye, Y. Hello, G. Huntzinger, D. Kouach, J. M. Reess, D. Tiphene, Y. Ghomchi, A. Coradini, F. Capaccioni, G. Arnold, and J. Benkhoff, "VIRTIS-H: a high-spectral-resolution channel for the Rosetta infrared imaging spectrometer," in *Infrared Spaceborne Remote Sensing VIII,* M. Strojnik and B. F. Andresen, eds., Proc. SPIE **4131,** 78–87 (2001).
7. D. P. Baldwin, D. S. Zamzow, and G. P. Miller, "AOTF–Echelle spectrometer for Air-ICP-AES continuous emission monitoring of heavy metals and Actinides," in *Environmental Monitoring and Remediation Technologies,* T. V. Dinh and R. L. Spellicy, eds., Proc. SPIE **3534,** 478–486 (1999).
8. U.S. Department of Energy, "Compact high resolution spectrometer," Innovative Technol. Summary Rep. OST/TMS ID 1564 (U.S. Department of Energy, 2000).
9. D. P. Baldwin, D. S. Zamzow, D. K. Ottesen, and H. A. Johnsen, "Testing of an echelle spectrometer as a LIBS detector at Sandia," Ames Laboratory Rep. IS-5148 (25 April 2001); www.osti.gov/bridge/servlets/purl/797630-w4wDHs/native/797630.pdf.
10. O. Korablev and J.-L. Bertaux, "High-resolution IR spectrometer for the studies of planetary atmospheres," Geophys. Res. Abs. Geophys. Instrum. **3,** 9492 (2001).
11. O. I. Korablev, J.-L. Bertaux, and I. I. Vinogradov, "Compact high-resolution IR spectrometer for atmospheric studies," in *infrared Spaceborne Remote Sensing,* M. Strojnik and B. F. Andresen, eds., Proc. SPIE **4818,** 272–281 (2002).
12. O. Korablev, J.-L. Bertaux, I. I. Vinogradov, Y. K. Kalinnikov,

D. Nevejans, E. Neefs, T. Le Barbu, G. Durry, A. Fedorova, and A. Grigoriev, "High resolution spectrometers for planetary spacecraft," presented at the EGS–AGU–EUG Joint Assembly, Nice, France, 6–11 April 2003.
13. O. Korablev, J.-L. Bertaux, D. Nevejans, and the SOIR instrument team, "Compact highresolution IR spectrometer for atmospheric studies," Geophys. Res. Abs. **5,** 14785 (2003).
14. O. I. Korablev, J.-L. Bertaux, I. I. Vinogradov, Y. K. Kalinnikov, D. Nevejans, E. Neefs, T. Le Barbu, and G. Durry, "Compact high-resolution echelle–AOTF NIR spectrometer for atmospheric measurements," in *Proceedings of the 5th International Conference on Space Optics (ICSO 2004),* B. Warmbein, ed. ESA Spec. Publ. SP-554 (European Space Agency, 2004), pp. 73–80.
15. O. Korablev, J.-L. Bertaux, I. I. Vinogradov, Y. K. Kalinnikov, D. Nevejans, E. Neefs, T. Le Barbu, G. Durry, A. Fedorova, and A. Grigoriev, "High resolution spectrometers for planetary spacecraft," presented at the 35th COSPAR Scientific Assembly, Paris, France, 18–25 July 2004.
16. H. Svedhem, "Venus Express science requirements document," ESA document VEX-RSSD-SP-002 (European Space Agency, 2004).
17. C. de Bergh, B. Bezard, T. Owen, D. Crisp, J. P. Maillard, and B. L. Lutz, "Deuterium on Venus–Observations from Earth," Science **251,** 547–549 (1 February 1991).
18. L. M. Mukhin, B. G. Gelman, N. I. Lamonov, V. V. Melnikov, D. F. Nenarokov, B. P. Okhotnikov, V. A. Rotin, and V. N. Khokhlov, "Gas-chromatographic analysis of the chemical composition of the Venusian atmosphere on the descent modules of the Venera-13 and Venera-14 probes," Kosm. Issled. **21,** 225–230 (1983).
19. V. I. Moroz, D. Spankuch, V. M. Linkin, W. Dohier, I. A. Matsygorin, K. Schafer, L. V. Zasova, D. Oertel, A. V. Dyachkov, R. Schuster, V. V. Kerzhanovich, H. Becker-Ross, E. A. Ustinov, and W. Stadthaus, "Venus spacecraft infrared radiance spectra and some aspects of their interpretation," Appl. Opt. **25,** (1986).
20. C. Palmer, *Diffraction Grating Handbook,* 6th ed. (Newport Corporation, 2005).
21. M. S. Gottlieb, "Acousto-optic tunable filters," in "*Design and Fabrication of Acousto-Optic Devices,*" A. P. Gotzoulis, D. R. Pape, and S. V. Kulakov, ed. Marcel Dekker, 197–283 (1994).
22. I. C. Chang, "Non-collinear acousto-optic filter with large angular aperture," Appl. Phys. Lett. **25,** 370–372 (1974).
23. B. W. Bach, Jr., K. G. Bach, M. Schulze, and B. Bach, Jr., "Modern echelons and echelles for infrared spectroscopy," in *Solar Physics and Space Weather Instrumentation*, S. Fineschi and R. Viereck, eds., Proc. SPIE **5901,** 184–190 (2005).
24. M. C. Hutley, *Diffraction gratings*, Vol. 6 of Techniques of Physics (Academic, 1982), p. 76.